

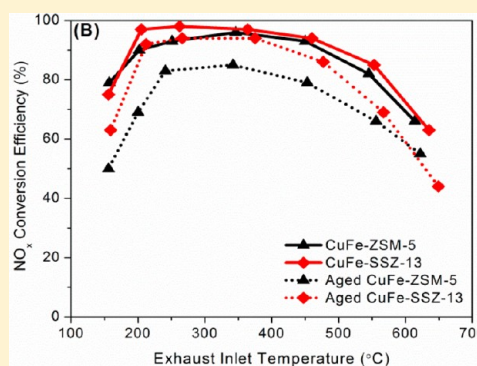
Heterometal Incorporation in Metal-Exchanged Zeolites Enables Low-Temperature Catalytic Activity of NO_x Reduction

Xiaofan Yang,[†] Zili Wu,^{‡,§} Melanie Moses-Debusk,[†] David R. Mullins,[§] Shannon M. Mahurin,[§] Robert A. Geiger,[†] Michelle Kidder,[§] and Chaitanya K. Narula^{*,†}

[†]Physical Chemistry of Materials, Materials Science & Technology Division, [‡]Center for Nanophase Materials Sciences, and [§]Chemical Science Division, Oak Ridge National Laboratory, One Bethel Valley Road, Oak Ridge, Tennessee 37831-6133, United States

Supporting Information

ABSTRACT: A series of new heterobimetallic zeolites has been synthesized by incorporating a secondary metal cation M (Sc³⁺, Fe³⁺, In³⁺, and La³⁺) in Cu-exchanged ZSM-5, zeolite- β , and SSZ-13 zeolites under carefully controlled experimental conditions. Characterization by diffuse-reflectance ultraviolet–visible spectroscopy (UV–vis), X-ray powder diffraction (XRD), extended X-ray absorption fine structure spectroscopy (EXAFS), and electron paramagnetic resonance spectroscopy (EPR) does not permit conclusive structural determination but supports the proposal that M³⁺ is hosted in zeolite structures in the vicinity of Cu(II), resulting in high NO_x conversion activity at 150 °C. Among various zeolites reported here, CuFe-SSZ-13 offers the best NO_x conversion activity in the 150–650 °C range and is hydrothermally stable when tested under accelerated aging conditions. Mechanistic studies employing stopped-flow diffuse reflectance FT-IR spectroscopy (DRIFTS) suggest that the high concentration of NO⁺ generated by heterobimetallic zeolites is probably responsible for their superior low-temperature NO_x activity.



1. INTRODUCTION

Zeolites play an indispensable role in a variety of industries, such as catalysis (FAU type), cements (natural zeolites), and detergents (LTA type), and recently their use in membranes and sensors is under rapid development.¹ Examples of successful applications of MFI- and CHA-type zeolites include their use as catalysts in fluid catalytic cracking (FCC), propane upgrading,² and NH₃-selective catalytic reduction (SCR) of NO_x for engine emission aftertreatment.^{3–5} The partial replacement of tetravalent silicon in zeolites with trivalent aluminum results in acidic sites that are responsible for catalytic activity.⁶ The efforts to tailor catalytic performance of zeolites include cation exchange, morphology modification of cage size and channel shape⁷ to increase the density of active acidic sites, and replacement of aluminum with boron (borosilicate)⁸ or gallium (galliosilicate)⁹ to tune the acidity of the active sites. Cation exchange, in general, offers an effective method to produce catalytic sites with mononuclear centers, although a dinuclear metallic core, Cu(μ -O)Cu, has been reported by Solomon and co-workers¹⁰ as the effective catalytic site for O₂ activation.

The race to be compliant with regulatory requirements for diesel engine emissions (or high air/fuel ratio lean-burn gasoline engines) led to extensive work on zeolites, and studies found Cu-ZSM-5^{3,11,12} and Fe-ZSM-5^{13–15} to be highly effective NH₃-SCR catalysts for NO_x reduction. The effective temperature ranges for Cu- and Fe-ZSM-5 are 250–450 and

350–650 °C,^{16,17} respectively. A variety of Fe-substituted zeolites have been investigated for NH₃-SCR activity, and their stability in catalyst operating conditions has been examined.^{18–20} The persistent gradual loss in activity of Cu- and Fe-ZSM-5 led to a search for a hydrothermally durable catalyst, resulting in the discovery of Cu-SSZ-13^{21–23} as a NH₃- or urea-SCR catalyst, which is now commercially available. Despite extensive efforts to improve the catalyst performance at low temperatures, including the use of alternative zeolites such as Cu-FAU²⁴ and Fe-Y,²⁵ a catalyst that could effectively reduce NO_x at 150 °C has remained elusive. Recent studies show that the NO_x conversion efficiency of a mixture of copper- and iron-substituted zeolites (ZSM-5 or SSZ-13) is an average of the performance of individual zeolites. In addition, sequential loading of copper- and iron-substituted zeolites does not lead to low-temperature activity.^{26,27}

As stated earlier, the effective oxygen activation over a copper-exchanged MFI zeolite¹⁰ closely resembles dinuclear metallic cores found in many important biological processes for small-molecule activation, such as the Cu(μ -O)₂Cu²⁸ core in “blue copper” for O₂ activation and the Fe(μ -O)₂Fe²⁹ core in methane monooxygenase (MMO) for methane activation. It can be reasoned that a zeolite with heterobimetallic dinuclear

Received: June 7, 2012

Revised: August 29, 2012

Published: October 9, 2012

core, provided it can be synthesized, can be used to tailor catalytic activity of a metal-exchanged zeolite due to both enhanced redox power and increased spin flexibility. Alternatively, if iron clusters (mono-, bi-, or oligonuclear species), generally proposed in overexchanged Fe-ZSM-5, can be incorporated in other zeolites, the resulting catalytic activity of heterobimetallic zeolites will depend on synergistic activity of both metal centers.^{30–38} These cluster interact with the cation through oxygen. We found that ion exchange does enable us to prepare heterobimetallic zeolites; however, the standard characterization tools do not enable the structure to be defined with certainty but support the proposal that the second metal is hosted in the zeolite structure. In this case, the iron (or other M^{3+}) species in zeolite cage will interact with Cu cation through a bridging oxygen. Recently, CuFe-ZSM-5 has been tested as one of the catalysts for direct oxidation of methane to methanol, and theoretical modeling suggests $[\text{Fe}_2(\mu_2\text{-OH})_2(\text{H}_2\text{O})_2]^{2+}$ as the diiron complex hosted in Cu-ZSM-5.³⁹

In this paper, we summarize our results on the synthesis of heterobimetallic zeolites, their preliminary structural characterization employing X-ray powder diffraction (XRD), diffuse-reflectance ultraviolet–visible spectroscopy (UV–vis), Fourier transform infrared spectroscopy (FT-IR), continuous-wave electron paramagnetic resonance spectroscopy (CW-EPR), extended X-ray absorption fine structure spectroscopy (EXAFS), and their catalytic activity for NO_x reduction under fast NH_3 -SCR conditions. Fast SCR tests provide the ideal test conditions for comparison of activities of various catalysts. The NO_x conversion efficiency of the best-performing catalyst, CuFe-SSZ-13, was also examined as a function of NO_2/NO_x ratio. The synthetic approach for ion exchange presented herein is quite generic and has enabled the introduction of a variety of trivalent cations as heteroatoms in Cu-ZSM-5, Cu-zeolite- β (Cu- β), and Cu-SSZ-13 under carefully controlled conditions. All heterobimetallic zeolites derived from Cu-ZSM-5 and Cu-SSZ-13 reduce NO_x by $\sim 80\%$ at 150°C . Like its parent zeolite, CuFe-SSZ-13 is hydrothermally stable under off-road engine aging cycles.

2. EXPERIMENTAL DETAILS

Samples of $\text{Cu}(\text{OOCCH}_3)_2\cdot\text{H}_2\text{O}$ were purchased from Sigma–Aldrich, and those of $\text{NH}_4\text{-ZSM-5}$ (CBV-2314, $\text{SiO}_2/\text{Al}_2\text{O}_3 = 23$), $\text{NH}_4\text{-zeolite-}\beta$ (CP814E, $\text{SiO}_2/\text{Al}_2\text{O}_3 = 25$), and Na-zeolite-Y (CBV-100, $\text{SiO}_2/\text{Al}_2\text{O}_3 = 5$) were from Zeolyst International. All purchased precursors were used as received. The pyrolysis and calcination of $\text{NH}_4\text{-ZSM-5}$ and $\text{NH}_4\text{-zeolite-}\beta$ at 500°C (heating rate $10^\circ\text{C}/\text{min}$, hold 4 h) furnished H-ZSM-5 and H- β , respectively. N,N,N -Trimethyladamantammmonium iodide⁴⁰ was prepared by a literature procedure for use as a template for the synthesis of H-SSZ-13.^{40,41}

Diffuse-reflectance UV–vis spectra were collected on a Cary 5000 UV–vis–NIR spectrophotometer under $R\%$ mode. FT-IR data were collected on a Bio-Rad FTS 575C spectrophotometer under $T\%$ mode from 4000 to 400 cm^{-1} . Temperature-programmed desorption (TPD) experiments were performed with a Quantachrome AutoSorb-1C instrument. Elemental analyses were performed by Galbraith Incorporated, Knoxville, TN. Powder X-ray diffraction data were obtained from a Scintag PAD V instrument.

Continuous-wave electron paramagnetic resonance (CW-EPR) measurements were obtained with an Elexsys E580 (Bruker) spectrometer operating in the X-band microwave frequency range. The microwave frequency was typically 9.66

GHz with a modulation frequency of 100 kHz . The modulation amplitude was set at 1 G for the large window scans and 10 G for the narrow window scans. The magnetic field was measured with a Hall probe, while the frequency was measured with a frequency counter. A Bruker ER4131VT variable-temperature unit was utilized to control the temperature of the sample, and spectra were acquired at 295 and 165 K . Samples were vacuum-sealed in standard quartz EPR tubes (Wilmad-LabGlass) with 4 mm outer diameter.

The X-ray absorption near-edge structure (XANES) and EXAFS spectroscopy of Cu and Fe were performed on beamline X19a at the National Synchrotron Light Source at the Cu K-edge (8979 eV) and the Fe K-edge (7112 eV). Spectra were measured at room temperature in He with no additional preparation. The samples ranged from 54 to 117 mg , mixed with approximately 100 mg of boron nitride (BN). The powder mixtures were pressed into 13 mm diameter pellets. Cu ($7.5\text{ }\mu\text{m}$) and Fe ($7.5\text{ }\mu\text{m}$) foils were mounted downstream of the samples and used for photon energy calibration. CuO was mixed with BN, pressed into a pellet, and measured for comparison. Simultaneous transmission and fluorescence detection was used.

In situ diffuse-reflectance Fourier transform infrared spectroscopy (DRIFTS) measurement was performed on a Nicolet Nexus 670 spectrometer equipped with a mercury–cadmium–telluride (MCT) detector, cooled by liquid nitrogen, and an in situ chamber (HC-900, Pike Technologies) with capability to heat samples to 900°C . The exiting stream was analyzed by an online quadrupole mass spectrometer (QMS) (OmniStar GSD-301 O_2 , Pfeiffer Vacuum).⁴² A combination of different gas compositions of NO (250 ppm), NO_2 (250 ppm), NH_3 (500 ppm), and O_2 (8.5%) was utilized in the DRIFTS mechanistic study employing a stop flow strategy as a mechanistic probe. The space velocity was kept constant at $50\,000\text{ h}^{-1}$. The catalyst was cleaned at 600°C under He for 30 min prior to each test. After cleaning, the sample was cooled to the desired temperature (150 or 250°C) and an IR background spectrum was collected. The sample was then subjected to a four-step treatment in sequence: (A) 15 min continuous flow of NO_x ($\text{NO}:\text{NO}_2 = 1:1$) and O_2 (8.5%), to allow for nitrite/nitrate formation and to reach an equilibrium between adsorbed and gas-phase NO_x ; (B) 15 min flow of pure He to remove gas-phase or loosely adsorbed/bound species on zeolite; (C) 15 min flow of NH_3 (500 ppm)/ O_2 (8.5%) to monitor the reactivity of tightly adsorbed/bound species; (D) flow of pure He with temperature ramping to 600°C ($20^\circ\text{C}/\text{min}$) to determine residual species. DRIFTS spectra were recorded for the entire process at a frequency of 71 scans per 15 min .

Catalyst powders were mixed with an equal amount (by weight) of inert cordierite and transferred to a benchtop reactor (Scheme S1, Supporting Information). A degreening process was done in a flow of $8.5\%\text{ O}_2$, $8.0\%\text{ CO}_2$, and $7.25\%\text{ H}_2\text{O}$ with balance N_2 at 600°C (inlet gas temperature) and a space velocity of $50\,000\text{ h}^{-1}$ for 2 h . NO_x conversion efficiency experiments employed simulated diesel exhaust containing $8.5\%\text{ O}_2$, $8.0\%\text{ CO}_2$, $7.25\%\text{ H}_2\text{O}$, 250 ppm NO_2 , 250 ppm NO , 500 ppm NH_3 , and N_2 as balance at a space velocity of $50\,000\text{ h}^{-1}$ and was evaluated in the 150 – 650°C temperature range.

Both monometallic and heterobimetallic metal exchanged zeolites were prepared by ion exchange in aqueous solution; details are available in Supporting Information. The synthesis of CuFe-SSZ-13 is a typical example of heterobimetallic zeolite and is described here. Cu-SSZ-13 (10.0 g) was suspended in an

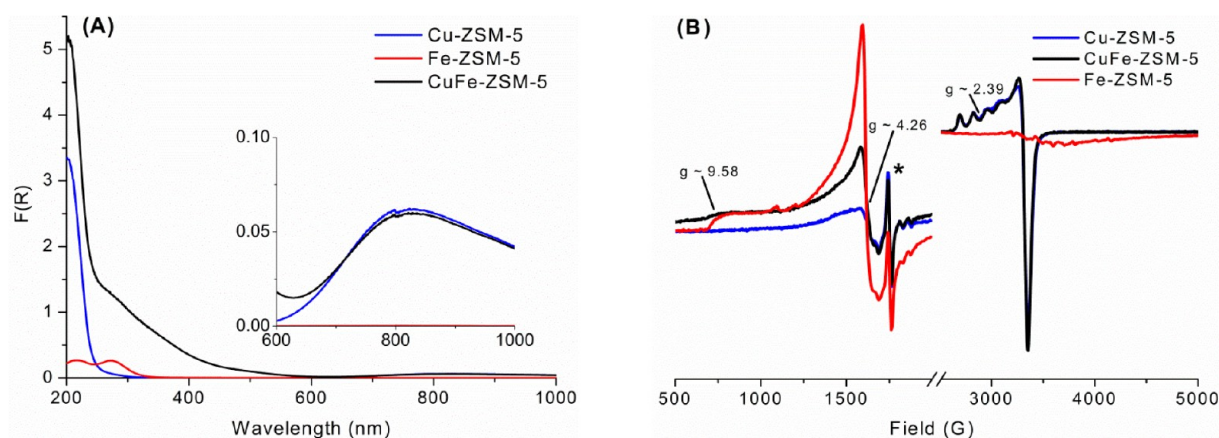


Figure 1. (A) Diffuse-reflectance UV-vis and (B) EPR spectra of Cu-, Fe-, and CuFe-ZSM-5. (The starred EPR signals are verified to originate from the resonator.)

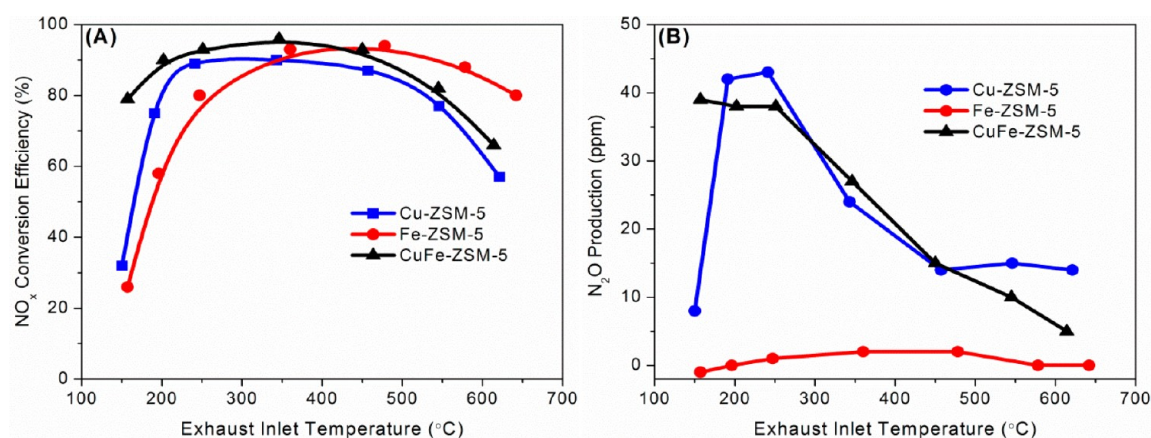


Figure 2. (A) NO_x conversion efficiency and (B) N_2O production patterns of CuFe-ZSM-5 compared to that of Cu- and Fe-ZSM-5, tested with simulated off-road diesel engine exhaust.

aqueous solution of 50 mL of 0.015 M $\text{Fe}(\text{NO}_3)_3$, degassed with N_2 , and kept stirring for 2 h at 80 $^{\circ}\text{C}$. Yellow solid was obtained after filtration, and the filtrate was clear and colorless. The product was then calcined in air at 500 $^{\circ}\text{C}$ (2 $^{\circ}\text{C}/\text{min}$) for 2 h to yield pale yellow CuFe-SSZ-13. Elemental analysis: Cu 2.71%, Fe 0.357%, Al 3.86%.

3. RESULTS AND DISCUSSION

Simple ion exchange of Cu-ZSM-5, Cu- β , and Cu-SSZ-13 with metal nitrate solutions results in the formation of heterobimetallic zeolites. The concentrations and temperature during ion exchange need to be carefully controlled to prevent formation of a mixture of monometallic zeolites. For example, the reaction of iron nitrate solution with Cu-ZSM-5 at 80 $^{\circ}\text{C}$ results in the incorporation of iron in the Cu-ZSM-5 structure. The blue Cu-ZSM-5 powder gradually turns yellow, and this product is separated by filtration, washed with water, dried in air, and calcined at 500 $^{\circ}\text{C}$ to obtain CuFe-ZSM-5 in high yields. Elemental analysis showed slight reduction in Cu content after exchange (2.76% vs 2.39%), quantitative incorporation of 0.4% Fe, and loss of Al (3.31% vs 2.97%). Increasing the temperature above 80 $^{\circ}\text{C}$ or increasing the ratio of iron nitrate salt to zeolites in the reaction mixtures leads to CuFe_x-ZSM-5-type materials, which shows loss of Cu without significant increase in iron incorporation.

The structural characterization of heterobimetallic zeolites with UV-vis, FT-IR, EPR, XRD, and EXAFS suggests that active iron is hosted in the zeolite, as reported previously for overexchanged iron ZSM-5 and CuFe-ZSM-5.^{30–38} X-ray powder diffraction of CuFe-ZSM-5 exhibits a typical MFI-zeolite diffraction pattern, suggesting that Fe^{3+} incorporation in Cu-ZSM-5 did not result in phase change or structural distortion (Figure S1, Supporting Information). The UV-vis spectrum of CuFe-ZSM-5 (Figure 1A) exhibits typical features of Cu-ZSM-5, which include a very intense absorption at ~ 200 nm and a broad peak at ~ 830 nm (Figure 1A, inset) from the charge transfer band related to $\text{O} \rightarrow \text{Cu}$ transition from lattice oxygen to isolated Cu^{2+} ions.⁴³ In addition, CuFe-ZSM-5 has two absorptions at 210 and 270 nm that are seen in Fe-ZSM-5-type structures.^{15,33} It is important to note that assignments of UV-vis absorption for Fe-ZSM-5 have remained a subject of discussion in literature. The bands <450 nm have been assigned to $\text{O}-\text{Fe}^{3+}$ by Tippins.⁴⁴ Schwidder et al.⁴⁵ assign the band at <300 nm to isolated Fe^{3+} , the band at 300–400 nm to oligomeric clusters, and the band at >400 nm to large Fe_2O_3 particles. The absorption in >450 nm region is due to d–d transition due to $\alpha\text{-Fe}_2\text{O}_3$.^{33,46} Lu et al.⁴⁶ assign the bands near 865, 670, and 560 nm to ground state, first excited state, and second excited state configurations of high-spin Fe^{3+} . Lu et al.⁴⁶ also note that the band near 560 nm is strongest and its actual position depends on the particle size of $\alpha\text{-Fe}_2\text{O}_3$.

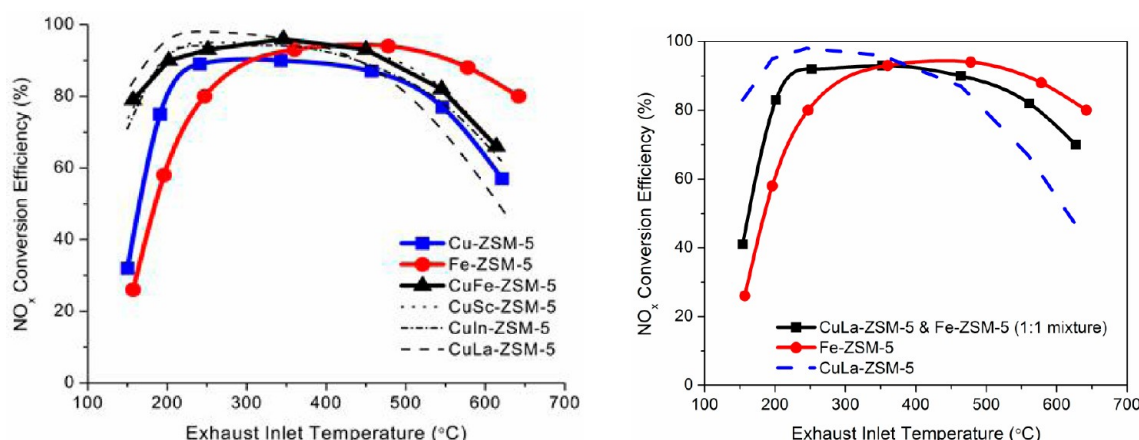


Figure 3. NO_x conversion efficiencies of (left) CuM-ZSM-5 (M = Sc, Fe, In, and La), compared with Cu- and Fe-ZSM-5, and (right) CuLa-ZSM-5, compared with Fe-ZSM-5 and a mixture of CuLa- and Fe-ZSM-5, tested with simulated off-road diesel engine exhaust.

Thus the absorption at 210 and 270 nm of our sample of CuFe-ZSM-5 can be assigned to O–Fe³⁺ and/or oligomeric clusters (e.g., [HO–Fe–O–Fe–OH]²⁺). There are no absorptions in >450 nm region for CuFe-ZSM-5 assignable to α-Fe₂O₃. FT-IR spectra of NH₄⁺, H-, Cu-, and CuFe-ZSM-5 do not show the characteristic framework band at 710–700 cm^{−1} suggesting extra-framework iron (Figure S2, Supporting Information).³⁹

EPR spectra of Cu- and Fe-ZSM-5 resemble those reported in literature (Figure 1B).^{15,43} EPR of CuFe-ZSM-5 (Figure 1B) is similar to that of Cu-ZSM-5 with a signal at *g* ~ 2.4 and resolved fine-hyperfine coupling, consistent with the experimentally observed square planar geometry.^{47–49} The higher EPR intensity of the signal at *g* ~ 4.3 of CuFe-ZSM-5 as compared with the signal in Cu-ZSM-5 suggests tetrahedral Fe³⁺, generally observed in EPR of Fe-ZSM-5,¹⁵ and supports the presence of Fe³⁺ in CuFe-ZSM-5.

The Cu EXAFS and XANES of CuFe-ZSM-5 are identical to those of Cu-ZSM-5 and the data suggest Cu to be Cu(II) (Figure S3, Supporting Information). The Fe EXAFS and XANES spectra of CuFe-ZSM-5 are also identical with those of Fe-ZSM-5. There is a fair amount of Fe–metal interaction in 2.0–3.5 Å, which has previously been ascribed to dimers and clusters.^{30–39} Thus, the results of UV–vis, FT-IR, EPR, and EXAFS support the proposed structure that involves a small oligomeric cluster of iron hosted in Cu-ZSM-5.

Catalytic efficiency testing of all catalysts described in this paper employed a fast SCR test protocol.⁵⁰ CuFe-ZSM-5 powder exhibits 80% NO_x conversion efficiency at 150 °C (Figure 2A) and maintains ~90% conversion efficiency in the 200–450 °C range, which drops to 68% at 650 °C. To our knowledge, CuFe-ZSM-5 is the first catalyst that can effectively reduce NO_x at 150 °C at 50 000 h^{−1} space velocity. In comparison, Cu-ZSM-5 shows only 30% NO_x conversion at 150 °C, which gradually increases to 90% at 250 °C but starts to drop below 90% at 450 °C and is 58% at 625 °C. Fe-ZSM-5 exhibits 90% NO_x conversion efficiency in the 350–550 °C range, which drops to ~80% at 650 °C. All three catalysts exhibit typical fast SCR behaviors, that is, correlated consumption of NH₃ and NO_x in ~1:1 ratio up to 400 °C (Figure S4, Supporting Information). The N₂ formation selectivity (Figure S5, Supporting Information) of CuFe-ZSM-5 is similar to that of Cu-ZSM-5. It is important to note that no NO_x reduction is observed in the absence of ammonia, suggesting that CuFe-ZSM-5 is not effective as a

NO_x reduction catalyst under oxidizing environment of diesel engine emissions (Figure S6, Supporting Information).

N₂O production (Figure 2B) during SCR with CuFe-ZSM-5 reaches maximum at 150 °C and then is identical to that of Cu-ZSM-5 in the 200–650 °C range. Fe-ZSM-5 does not produce N₂O during the SCR catalytic cycle. Recent report from Yang and co-workers⁵¹ clearly shows that a mixture of Cu- and Fe-ZSM-5 exhibits NO_x conversion activity that is an average of individual component NO_x conversion activities. Metkar et al.⁵² investigated NO_x conversion activity of Cu- and Fe-zeolite catalysts in various configurations but did not observe low-temperature activity under standard or fast SCR conditions. Thus, our catalyst, CuFe-ZSM-5, is definitely not a mixture of Cu- and Fe-ZSM-5, and the low-temperature reactivity of CuFe-ZSM-5 can be attributed to a synergistic effect resulting from the incorporation of Fe³⁺ in close proximity to Cu²⁺.

3.1. Generality of Ion Exchange for Synthesis of Heterobimetallic Zeolites. Successful incorporation of Fe³⁺ into Cu-ZSM-5 (i.e., CuFe-ZSM-5), resulting in enhanced low-temperature NO_x reduction efficiency, prompted us to explore the generality of the method for synthesis of other heterobimetallic zeolites. We selected Sc³⁺, In³⁺, and La³⁺ on the basis of their preferred 3+ oxidation states under oxidizing environment. Furthermore, these elements represent different electronic configurations. Sc³⁺ has no d electrons with five empty d orbitals, enabling it to interact with Cu²⁺ via bridging oxo atoms or direct metal–metal interaction; all of the In³⁺ d orbitals are fully occupied, preventing direct metal–metal interaction with Cu²⁺ centers; and La³⁺ can interact with Cu²⁺ via d–f exchange.⁵³ Thus, one can expect varying catalytic activity due to varying electronic influence over the Cu²⁺ center.

Degree of heteroatom incorporation in Cu-ZSM-5 varies among these elements, and incorporation of In³⁺, Sc³⁺, and La³⁺ decreases with increasing ionic radius of these heteroatoms. All new catalysts exhibit identical ZSM-5 powder diffraction patterns (Figure S1, Supporting Information). Subtle changes observed in the NH₃ TPD spectra (Figure S7, Supporting Information) of these catalysts may be a result of the small concentrations of the trivalent element or increased hindrance for NH₃ interaction due to heteroatom incorporation. As expected (Figure S8, Supporting Information), the UV–vis spectra of CuSc- and CuLa-ZSM-5 are essentially identical to that of Cu-ZSM-5. CuIn-ZSM-5 is also identical to Cu-ZSM-5 except it exhibits an additional absorption at ~300 nm. It is

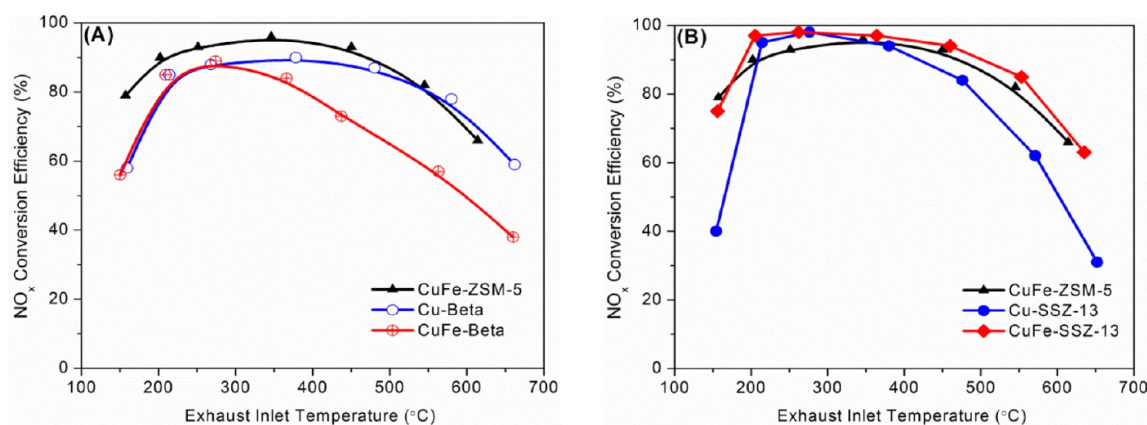


Figure 4. NO_x conversion efficiency of (A) CuFe-ZSM-5, Cu- β , and CuFe- β and (B) CuFe-ZSM-5, Cu-SSZ-13, and CuFe-SSZ-13.

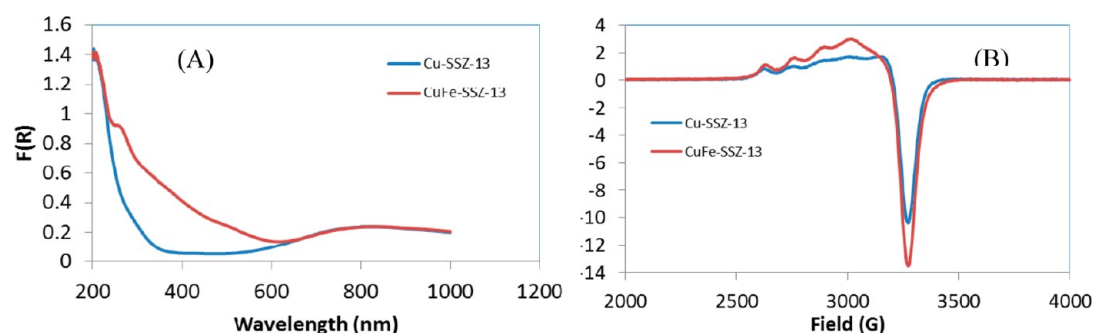


Figure 5. (A) Diffuse-reflectance UV-vis and (B) EPR spectra of Cu- and CuFe-SSZ-13 at 170 K.

important to note that nanoscale In_2O_3 also exhibits strong absorption around 300 nm.^{54,55}

All new heterobimetallic MFI-zeolite catalysts, CuM-ZSM-5, consistently exhibit $>70\%$ NO_x conversion efficiency at 150°C , maintain $\sim 90\%$ conversion efficiency in the $200\text{--}450^\circ\text{C}$ range, and exhibit a drop to $\sim 60\%$ above 600°C (Figure 3, left). Lanthanide-containing CuLa-ZSM-5 has the best low-temperature performance, but its efficiency also has the largest change after 500°C . The NO_x conversion efficiency of a 1:1 mixture of CuLa-ZSM-5 mixed with Fe-ZSM-5 is shown in Figure 3 (right) along with the NO_x conversion efficiency of CuLa- and Fe-ZSM-5. The activity of the mechanical mixture closely follows the average of the two parent zeolites, not exceeding the performance of CuLa-ZSM-5 at low temperature or the performance of Fe-ZSM-5 at high temperature. This result, coupled with the recently published reports on mixtures of copper and iron ZSM-5 and SSZ-13, clearly rule out our bimetallic zeolites being a mechanical mixture.

3.2. Effects of Zeolite Framework. We selected Cu- β (BEA) and Cu-SSZ-13 (CHA), which have also been explored as SCR catalysts,^{21–23} to gain insights into framework effects. The framework structure of zeolite- β remains intact after the sequential solution exchange with Cu^{2+} and Fe^{3+} as indicated by the XRD powder diffraction pattern (Figure S9, Supporting Information). UV-vis spectra (Figure S10, Supporting Information) of Cu- β and CuFe- β resemble those of Cu- and CuFe-ZSM-5, respectively. The charge-transfer band $\text{O} \rightarrow \text{Cu}$ near 800 nm is present in both Cu- β and CuFe- β . In addition to all the absorptions of Cu- β , CuFe- β also exhibits three extra absorptions at 270 , 360 , and 500 nm , which are assigned to extra-framework octahedral Fe^{3+} , small oligomeric clusters, and iron oxides, respectively.

The presence of iron in CuFe- β does not result in enhanced NO_x conversion efficiency (Figure 4A) when compared to Cu- β at 150°C . Between 200 and 250°C , CuFe- β shows identical NO_x reduction efficiency as Cu- β , and both are comparable with CuFe-ZSM-5. Above 250°C , CuFe- β gradually loses its NO_x conversion capability, while Cu- β maintains a NO_x conversion curve parallel to but slightly below that of CuFe-ZSM-5. It is possible that the lack of a square planar coordination environment in zeolite, identified to be the preferred Cu binding site in ZSM-5, hampers the effective function of the heterometallic Cu/Fe core to boost the low-temperature NO_x conversion efficiency.

As indicated by XRD powder diffraction pattern, the framework structure of Cu-SSZ-13 remains intact after the sequential solution exchange with Cu^{2+} and Fe^{3+} (Figure S11, Supporting Information). The UV-vis spectra of CuFe- and Cu-SSZ-13 exhibit a very intense absorption from a d-d transition at $\sim 210\text{ nm}$ and a broad peak at $\sim 830\text{ nm}$ (Figure 5A) from the charge-transfer band related to $\text{O} \rightarrow \text{Cu}$ transition from lattice oxygen to isolated Cu^{2+} ions.⁵⁶ In addition, CuFe-SSZ-13 has two absorptions that can be attributed to isolated tetrahedral and octahedral Fe^{3+} at 210 and 270 nm , respectively, as seen in Fe-ZSM-5-type structures.^{15,33} In general, absorptions of iron oxide clusters and iron oxide particles are believed to be above 400 nm ¹⁵ and are not seen.

A new, intense absorption centered at $\sim 350\text{ nm}$ is also present, which could be assigned to octahedral Fe^{3+} in small oligomeric clusters and has previously been assigned to $[\text{HO-Fe-O-Fe-OH}]^{2+}$ cluster bound to the zeolite framework via iron oxygen bridges in overexchanged Fe-ZSM-5.¹⁵ EPR spectra of Cu-SSZ-13 (Figure 5B) and CuFe-ZSM-5 (Figure 1B) are similar to that of Cu-ZSM-5 with a signal at $g \sim 2.4$ and

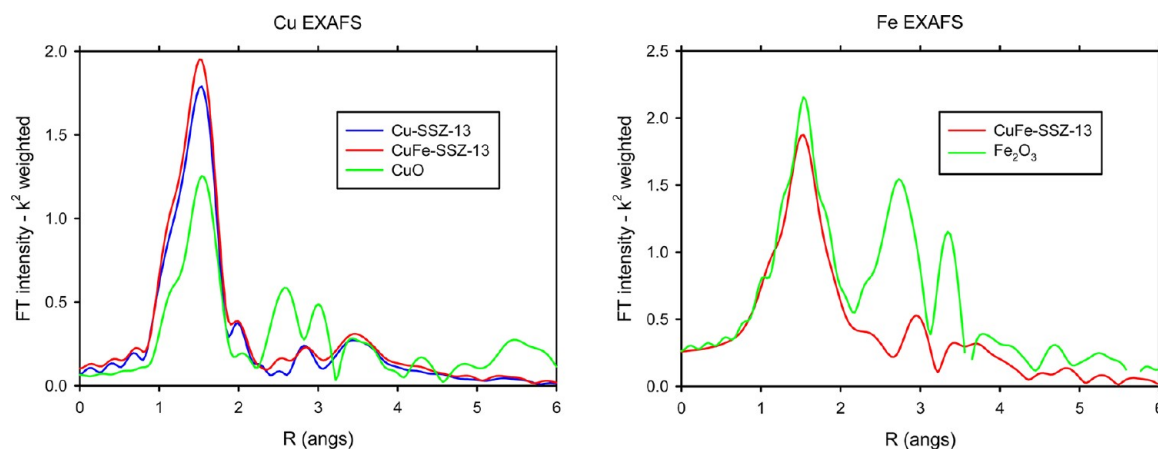


Figure 6. EXAFS spectra of Cu-SSZ-13 and CuFe-SSZ-13.

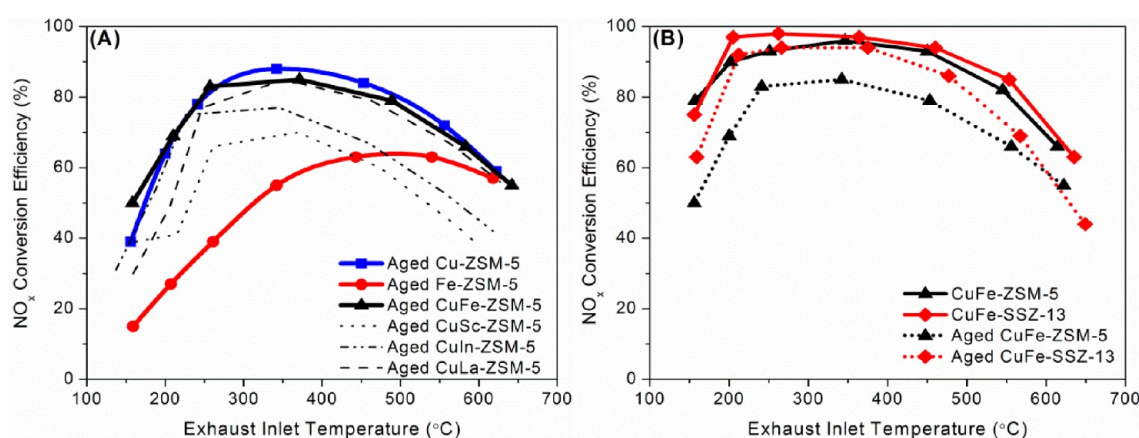


Figure 7. NO_x conversion efficiency of (A) CuM-ZSM-5 (B) CuFe-ZSM-5 and CuFeSSZ-13 after hydrothermal aging.

resolved fine-hyperfine coupling, consistent with the experimentally observed square planar geometry.^{47–49}

The features of EXAFS and XANES spectra of Cu-SSZ-13 are identical to the ones reported in literature and support Cu(II) oxidation state.^{56–58} As noted for ZSM-5 zeolites, the Cu EXAFS and XANES spectra (Figure 6) of CuFe-SSZ-13 are identical to those of Cu-SSZ-13 and the data suggest Cu to be Cu(II). The Fe EXAFS and XANES spectra of CuFe-SSZ-13 are identical to those of Fe-SSZ-13. In analogy with Fe-ZSM-5, we assign Fe–metal interaction in 2.0–3.5 Å to dimers and clusters.^{30–39} Thus, the results of UV–vis, FT-IR, EPR, and EXAFS support the proposed structure that involves small oligomeric cluster of iron hosted in Cu-SSZ-13.

CuFe-SSZ-13 exhibits high NO_x reduction efficiency at low temperature reminiscent of CuFe-ZSM-5 (Figure 7B). In addition, the N₂O production from CuFe-SSZ-13 is 50% less than that from CuFe-ZSM-5 at the peak value [Figure S13 (left), Supporting Information]. This result can be attributed to the unique framework of SSZ-13, which also possesses suitable locations of perfect square planar coordination environments to host Cu²⁺. Recent reports in the literature show that the NO_x conversion activity of a mixture of Cu- and Fe-SSZ-13 is an average of the individual activities of Cu- and Fe-SSZ-13.⁵¹ High NO_x conversion activity of our CuFe-SSZ-13 catalyst, therefore, is not due to it being a mixture of Cu- and Fe-SSZ-13. Lower NO₂ in NO_x has an impact on the NO_x conversion at low temperature, and only 42% NO_x conversion is observed when there is no NO₂ in NO_x. Increasing the NO₂/NO_x ratio

to 0.1, 0.25, 0.4, and 0.5 results in 55%, 66%, 68%, and 72% NO_x conversion at 160 °C [Figure S13 (right), Supporting Information].

3.3. Hydrothermal Stability. We carried out accelerated aging by employing a protocol that exposes catalyst to 675 °C for 50 h under a flow of air containing 10% water. The zeolite catalysts are well-known to deteriorate gradually via dealumination under emission treatment conditions, resulting in the loss of catalytic sites.^{59–61} X-ray powder diffraction patterns of all catalysts, described in this study, show that the zeolite framework is retained after accelerated aging, but the aging does result in the partial loss of NO_x reduction performance (Figure 7). Fe-ZSM-5 shows at least 20% loss of NO_x conversion activity over the entire testing temperature range. Cu-ZSM-5 retains ~80% NO_x conversion between 250 and 450 °C. The observed efficiency loss of Cu- and Fe-ZSM-5 is consistent with the loss of efficiency observed upon subjecting these zeolites to accelerated aging under on-road diesel engine conditions.^{61–63}

The introduction of heteroatoms in ZSM-5 structure neither enhances nor reduces hydrothermal stability of MFI zeolites. The hydrothermal stability of CuM-ZSM-5 resembles that of Cu-ZSM-5. Chabazites [CHA], on the other hand, exhibit remarkable hydrothermal durability. The durability of Cu-SSZ-13 is not adversely impacted by incorporation of iron. Interestingly, the low-temperature activity of CuFe-SSZ-13 experiences a moderate drop at 150 °C, but there is negligible change in the 200–450 °C range (Figure 7B). It is likely that

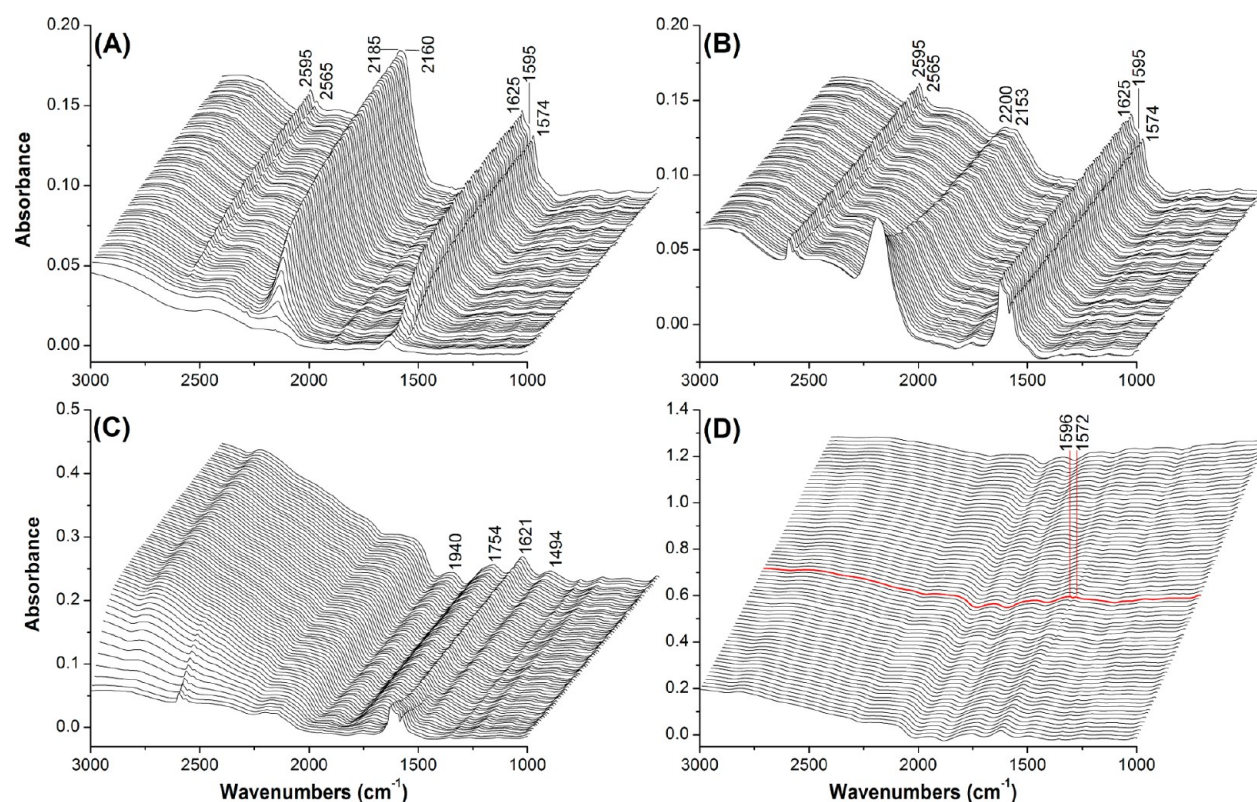


Figure 8. DRIFTS spectra of Cu-SSZ-13 at 150 °C during the four-step treatment: (A) NO_x/O_2 flow, (B) He purging, (C) NH_3/O_2 flow, and (D) desorption in He with temperature ramping to 600 °C. Each step takes 15 min.

the smaller pores of Cu-SSZ-13 prevent iron oxide cluster migration from pores. Thus, CuFe-SSZ-13 is the best catalyst among all catalysts reported in this study, based on its NO_x conversion performance in the 150–650 °C range and its hydrothermal stability.

3.4. Mechanistic Studies. We carried out mechanistic studies with the expectation that we might gain insights into synergistic effects of heteroatom incorporation in zeolite structure by utilizing in situ DRIFTS. Our studies build on previous mechanistic studies, including reports from Sachtler and co-workers on NO adsorption on Fe-MFI⁶⁴ and BaNa-Y⁶⁵ and from Chen and co-workers⁶⁶ on differences between copper- and iron-based zeolite (ZSM-5) in NH_3 -SCR.

After the initial contact with NO_x/O_2 (step 1) at 150 °C (Figure 8A), Cu-SSZ-13 displays peaks at 1574, 1595, and 1625 cm^{-1} , which can be assigned to nitrite/nitrate adsorbed on zeolites⁶⁴ and which gradually increase in intensity as a function of time. In addition, a fast-growing peak is observed at 2160 cm^{-1} accompanied by a second peak at 2185 cm^{-1} after 2 min. Both merge to a broad double-shouldered peak centered at 2170 cm^{-1} , which can be assigned to NO^+ either adsorbed on zeolites or compounded with $\text{NO}_2/\text{N}_2\text{O}_4$.^{65,67,68} If NO_2 and O_2 are excluded from the gas input, the 2170 cm^{-1} peak is suppressed and the peaks associated with NO_2 are not observed (Figure S14, Supporting Information). Low-intensity peaks at 2565 and 2595 cm^{-1} (with a broad shoulder) are also observed and assigned to adsorbed nitrates/nitrites due to the synchronic behavior with those fully identified peaks associated with nitrates/nitrites at 1574, 1595, and 1625 cm^{-1} . After replacement of NO_x/O_2 flow with He, the nitrate/nitrite peaks (1574, 1595, and 1625 cm^{-1}), as well as the low-intensity peaks at 2565 and 2595 cm^{-1} , remain unchanged, but the 2170

cm^{-1} peak is completely depleted, suggesting weak adsorption of the NO^+ species on zeolite surface (Figure 8B). The nitrate/nitrite peak heights (1574, 1595, and 1625 cm^{-1}) remain unchanged during thermal treatment up to 500 °C (Figure S15, Supporting Information).

After ammonia flow is started, there is time delay of ~ 1 min before the depletion of nitrate/nitrite-associated peaks at 1574 and 1595 cm^{-1} (Figure 8C). This suggests that the zeolite skeleton adsorbs NH_3 until saturation on the active metal sites for the catalysis. The nitrate/nitrite peaks completely vanish by the end of the ammonia treatment cycle. At the end of the ammonia treatment cycle, the spectrum resembles that of ammonia-treated parent zeolite (Figure S16, Supporting Information) and the four adsorption peaks between 1400 and 2000 cm^{-1} are due to strongly adsorbed NH_3 species. The intensity of these peaks does not change even after heating to 600 °C in the flow of He in the last step (Figure 8D). During heating in the last step, two peaks at 1572 and 1596 cm^{-1} reappear at about 300 °C, suggesting the presence of adsorbed nitrate/nitrite. This occurrence must be due to the migration of NO_x from inactive sites in the zeolite structure to catalytically active sites. As adsorbed ammonia reaches these sites, the formation of N_2 and H_2O is also observed from online mass spectrometry due to NO_x reduction.

Increasing the NO_x/O_2 reaction temperature to 250 °C results in no significant change except the NO^+ species peaks are less intense than those for nitrite/nitrate and additional weak bands are observed at 1389, 1357, and 1256 cm^{-1} (Figure S17A, Supporting Information), previously assigned to surface nitrate/nitrite.⁶⁵ The He cleaning step results in a faster disappearance of NO^+ species peaks (Figure S17B, Supporting

Information) but the weak bands at 1389, 1357, and 1256 cm^{-1} remain unchanged.

The spectrum of the new catalyst, CuFe-SSZ-13, is almost identical to that of Cu-SSZ-13 during all four steps of treatment at 150 °C except that the NO^+ peak is nearly twice as intense for CuFe-SSZ-13 (Figure 9) and a higher proportion of this

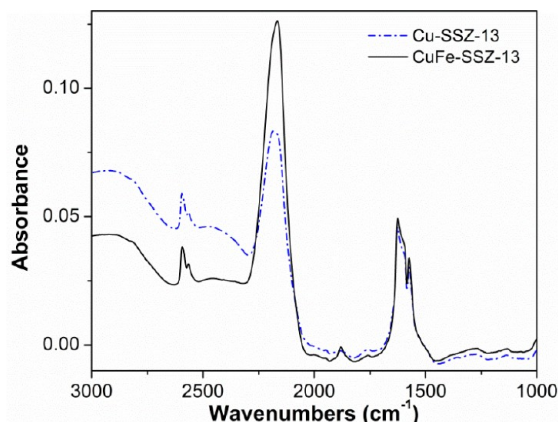


Figure 9. DRIFTS spectra of CuFe- and Cu-SSZ-13 treated by NO_x/O_2 at 150 °C.

peak remains after the He purge step (Figure S18B, Supporting Information). A slight enhancement in the intensity of peak at 1881 cm^{-1} is also observed. Increasing the NO_x/O_2 reaction temperature to 250 °C in step 1 makes the IR spectra of CuFe-SSZ-13 identical to those of Cu-SSZ-13 (Figure S19, Supporting Information). Thus, it is possible that there is a correlation between high NO_x reduction activity and the enhanced formation of NO^+ at 150 °C. Since NO^+ species is retained even after the He purge, it is probably linearly bound to the Cu center in a weak mode rather than being present only in the gas phase as suggested by Sachtler and co-workers.⁶⁵

Our results suggest that NO^+ plays an important role in fast SCR reaction, and the high catalytic activity of heterobimetallic zeolites at 150 °C can be attributed to the high NO^+ concentration as compared with monometallic zeolites. This is in contrast with earlier postulation^{64,65} that attributed NO_x reduction under fast SCR conditions to N_2O_3 , which can form as an intermediate in the gas-phase equilibrium of NO and NO_2 , and can react with 2 equiv of NH_3 to yield ammonium nitrite (NH_4NO_2) that decomposes to N_2 and H_2O near 100 °C.

In our study, the formation of N_2O_3 with IR peaks at 1879, 1578, and 1297 cm^{-1} , as reported by Sachtler and co-workers,⁶⁴ is not dominant. The generation of adsorbed NO^+ species has been shown by Sachtler and co-workers,⁶⁵ who suggested that N_2O_4 , a dimer of NO_2 , disproportionates to NO^+ and NO_3^- over the catalyst. Our results are more aligned with this observation. The overall fast-SCR reaction scheme can be summarized as shown in Figure 10A.

The pathway of NO^+ reduction by NH_3 to N_2 has been proposed by previous theoretical^{69–73} and experimental^{74–76} studies to involve unstable intermediate nitrosamide, H_2NNO .

The enhanced NO_x reduction at 150 °C by heterobimetallic zeolites must originate from the higher concentrations of NO^+ at 150 °C, while nitrite/nitrate formation remains unchanged as compared with parent monometallic zeolites. It is likely that the enhanced NO^+ generation occurs at the Cu sites with high valence, that is, Cu(III). O_2 may provide sufficient oxidation

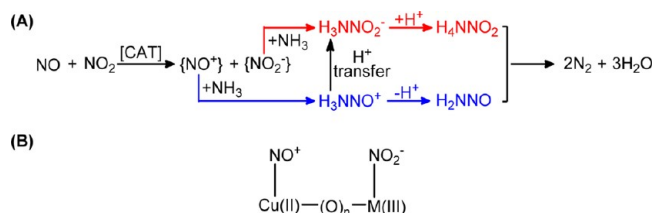


Figure 10. Fast-SCR reaction intermediates.

power to generate Cu(III) as demonstrated by a square planar copper complex.⁷⁷ Introduction of a redox-active metal into the vicinity of the active copper center can strengthen the weak interaction between Cu(III) and NO^+ . In addition, a heterobimetallic site can promote the disproportionation reaction between NO and NO_2 (Figure 10B) even in the absence of an external oxidant to generate transient Cu(III) based on the asymmetric structure motif to gain additional free energy when compared to a homogeneous bimetallic core by hosting NO_2^- at the higher charged metal M(III) and NO^+ at the Cu(II) site. These assumptions explain the dependence of the degree of low-temperature NO_x conversion on redox properties of heteroatom in our heterobimetallic zeolites where La-, Fe-, Sc-, and In-incorporated zeolites exhibit 83%, 79%, 74%, and 71% NO_x conversion at 150 °C, respectively.

4. CONCLUSIONS

We have shown that hydrothermally stable heterobimetallic zeolites can be easily prepared by ion exchange of monometallic zeolites. The heterobimetallic zeolites offer the additional advantage of low-temperature NO_x conversion activity as compared with the parent monometallic zeolites. The characterization data from diffuse-reflectance UV–vis, FT-IR, XRD, EXAFS, and EPR do not permit conclusive structural determination but supports the proposal that M^{3+} is hosted in the zeolite structure. The enhanced reactivity of the parent zeolite with heteroatom incorporation suggests that heteroatom is in the vicinity of Cu(II). Mechanistic studies suggest that the origin of low-temperature reactivity is related to the production and retention of the NO^+ species. It is likely that a heterobimetallic core facilitates the disproportionation reaction between NO and NO_2 to form and stabilize NO^+ and NO_2^- .

■ ASSOCIATED CONTENT

Supporting Information

Additional text, one scheme, and 19 figures showing synthesis of metal-exchanged zeolites and XRD, FT-IR, UV–vis, NH_3 TPD, XANES, EXAFS, and in situ DRIFTS spectra of new heterobimetallic zeolites described in this paper. This material is available free of charge via the Internet at <http://pubs.acs.org>.

■ AUTHOR INFORMATION

Corresponding Author

*E-mail narulack@ornl.gov.

Notes

The authors declare no competing financial interest.

■ ACKNOWLEDGMENTS

This research is sponsored by the U.S. Department of Energy, Office of Energy Efficiency and Renewable Energy, Advanced Manufacturing Office, Office of Vehicle Technology under Propulsion Materials Program, and Office of Basic Energy

Sciences under Contract DE-AC05-00OR22725 with UT-Battelle, LLC. We thank Dr. G. Brown for assistance in UV-vis data acquisition. The DRIFTS work was performed at the Center for Nanophase Materials Sciences, which is sponsored at Oak Ridge National Laboratory by the Scientific User Facilities Division, Office of Basic Energy Sciences, and U.S. Department of Energy. Use of the National Synchrotron Light Source, Brookhaven National Laboratory, was supported by the US Department of Energy, Office of Science, Office of Basic Energy Sciences, under Contract No. DE-AC02-98CH10886.

REFERENCES

- (1) *Introduction to Zeolite Science and Practice*, 3rd ed.; Cejka, J., Bekkum, H., Corma, A., Schuth, F., Eds.; Studies in Surface Science and Catalysis, Vol 168; Elsevier: Amsterdam, 2007.
- (2) Tanabe, K.; Holderich, W. F. *Appl. Catal., A* **1999**, *181*, 399–434.
- (3) Palella, B. I.; Lisis, L.; Pirone, R.; Russo, G.; Notaro, M. *Kinet. Catal.* **2006**, *47*, 728–736.
- (4) Joyner, R.; Stockenhuber, M. *J. Phys. Chem. B* **1999**, *103*, 5963–5976.
- (5) Zecchina, A.; Rivallan, M.; Berlier, G.; Lamberti, C.; Ricchiardi, G. *Phys. Chem. Chem. Phys.* **2007**, *9*, 3483–3499.
- (6) Guisnet, M.; Gnep, N. S.; Alario, F. *Appl. Catal., A* **1992**, *89*, 1–30.
- (7) Cantin, A.; Corma, A.; Diaz-Cabanas, M. J.; Jorda, J. L.; Moliner, M. *J. Am. Chem. Soc.* **2006**, *128*, 4216–4217.
- (8) Hong, S. B.; Uh, Y. S.; Woo, S. I.; Lee, J. K. *Korean J. Chem. Eng.* **1991**, *8*, 1–5.
- (9) Liu, X. S.; Klinowski, J. *J. Phys. Chem.* **1992**, *96*, 3403–3408.
- (10) Woertink, J. S.; Smeets, P. J.; Groothaert, M. H.; Vance, M. A.; Sels, B. F.; Schoonheydt, R. A.; Solomon, E. I. *Proc. Natl. Acad. Sci. U.S.A.* **2009**, *106*, 18908–18913.
- (11) Komatsu, T.; Nunokawa, M.; Moon, I. S.; Takahara, T.; Namba, S.; Yashima, T. *J. Catal.* **1994**, *148*, 427–437.
- (12) Iwamoto, M.; Furukawa, H.; Mine, Y.; Uemura, F.; Mikuriya, S. I.; Kagawa, S. *J. Chem. Soc., Chem. Commun.* **1986**, 1272–1273.
- (13) Long, R. Q.; Yang, R. T. *J. Am. Chem. Soc.* **1999**, *121*, 5595–5596.
- (14) Komatsu, T.; Uddin, M. A.; Yashima, T. *Zeolite: A Refined Tool for Designing Catalytic Sites*; Elsevier: Amsterdam, 1995.
- (15) Devdas, M.; Krocher, O.; Elsener, M.; Wokaun, A.; Mitrikas, G.; Soger, N.; Pfeifer, M.; Demel, Y.; Mussmann, L. *Catal. Today* **2007**, *119*, 137–144.
- (16) Cavatio, G.; Girard, J.; Patterson, J.; Montreuil, C.; Cheng, Y.; Lambert, C., SAE Paper 07PFL-643.
- (17) Cavatio, G.; Jen, H. W.; Warner, J. R.; Girard, J. W.; Kim, J. Y.; Lambert, C. K., SAE Paper 08PFL-723.
- (18) Ma, L.; Li, J.; Cheng, Y.; Lambert, C. K.; Fu, L. *Environ. Sci. Technol.* **2012**, *46*, 1747–1754.
- (19) Ma, L.; Li, J.; Arandiyán, H.; Shi, W.; Liu, C.; Fu, L. *Catal. Today* **2012**, *184*, 145.
- (20) Li, J. H.; Zhu, R.; Cheng, Y.; Lambert, C. K.; Yang, R. T. *Environ. Sci. Technol.* **2010**, *44*, 1799.
- (21) Bull, I.; Xue, W.; Burk, P.; Boorse, S. R.; Jaglowski, W. M.; Koermer, G. S.; Moini, A.; Patchett, J. A.; Dettling, J. C.; Caudle, M. T. U.S. Patent 7,601,662, 2009.
- (22) Korhonen, S. T.; Fickel, D. W.; Lobo, R. F.; Weckhuysen, B. M.; Beale, A. M. *Chem. Commun.* **2011**, *47*, 800–802.
- (23) Kwak, J. H.; Tonkyn, R. G.; Kim, D. H.; Szanyi, J.; Peden, C. H. F. *J. Catal.* **2010**, *275*, 187–190.
- (24) Kieger, S.; Delahay, G.; Coq, B.; Neveu, B. *J. Catal.* **1999**, *183*, 267–280.
- (25) Amiridis, M. D.; Puglisi, F.; Dumesic, J. A.; Millman, W. S.; Topsoe, N. Y. *J. Catal.* **1993**, *142*, 572–584.
- (26) Ye, Q.; Wang, L.; Yang, R. T. *Appl. Catal., A* **2012**, *427*, 24.
- (27) Metkar, P. S.; Harold, M. P.; Balakotaiah, V. *Appl. Catal., B* **2012**, *111–112*, 67.
- (28) Deng, H. B.; Hoffmann, R. *Angew. Chem., Int. Ed.* **1993**, *32*, 1062–1065.
- (29) Baik, M. H.; Newcomb, M.; Friesner, R. A.; Lippard, S. J. *Chem. Rev.* **2003**, *103*, 2385–2419.
- (30) Battiston, A. A.; Bitter, J. H.; Heijboer, W. M.; de Groot, F. M. F.; Koningsberger, D. C. *J. Catal.* **2003**, *215*, 279–293.
- (31) Jia, J.; Sun, Q.; Wen, B.; Chen, L. X.; Sachtler, W. M. H. *Catal. Lett.* **2002**, *82*, 7–11.
- (32) Battiston, A. A.; Bitter, J. H.; Koningsberger, D. C. *J. Catal.* **2003**, *218*, 163–177.
- (33) Kumar, M. S.; Schwidder, M.; Grüner, W.; Brückner, A. *J. Catal.* **2004**, *227*, 384–397.
- (34) Xia, H.; Sun, K.; Feng, Z.; Li, W. X.; Li, C. *J. Phys. Chem. C* **2008**, *112*, 9001.
- (35) Pirngruber, G. D.; Roy, P. K.; Prins, R. *Phys. Chem. Chem. Phys.* **2006**, *8*, 3939.
- (36) Battiston, A. A.; Bitter, J. H.; Koningsberger, D. C. *Catal. Lett.* **2006**, *66*, 75.
- (37) Sun, K.; Xia, H.; Hensen, E.; van Santen, R.; Li, C. *J. Catal.* **2006**, *238*, 186.
- (38) Lobree, L. J.; Hwang, I.-C.; Reimer, J. A.; Bell, A. T. *J. Catal.* **1999**, *186*, 242.
- (39) Hammond, C.; Forde, M. M.; Rahim, M. H. A.; Thetford, A.; He, Q.; Jenkins, R. L.; Dimitratos, N.; Lopez-Sanchez, J. A.; Dummer, N. F.; Murphy, D. M.; Carley, A. F.; Taylor, S. H.; Willock, D. J.; Stangland, E. E.; Kang, J.; Hagen, H.; Kiely, C. J.; Hutchings, G. J. *Angew. Chem., Int. Ed.* **2012**, *51*, 5129–5133.
- (40) Zones, S. I. U.S. Patent 4544538, 1985.
- (41) Fickel, D. W.; Fedeyko, J. M.; Lobo, R. F. *J. Phys. Chem. C* **2010**, *114*, 1633–1640.
- (42) Wu, Z. L.; Zhou, S. H.; Zhu, H. G.; Dai, S.; Overbury, S. H. *J. Phys. Chem. C* **2009**, *113*, 3726–3734.
- (43) Ismagilov, Z. R.; Yashnik, S. A.; Anufrienko, V. F.; Larina, T. V.; Vasenin, N. T.; Bulgakov, N. N.; Vosel, S. V.; Tsykoza, L. T. *Appl. Surf. Sci.* **2004**, *226*, 88–93.
- (44) Tippin, H. H. *Phys. Rev. B* **1970**, *1*, 126.
- (45) Schwidder, M.; Kumar, M. S.; Klementiev, K.; Pohl, M. M.; Bruckner, A.; Grunert, W. *J. Catal.* **2005**, *231*, 314.
- (46) Lu, L.; Li, L.; Wang, X.; Li, G. *J. Phys. Chem. B* **2005**, *109*, 17151.
- (47) Kucherov, A. V.; Slinkin, A. A.; Kondratiev, D. A.; Bondarenko, T. N.; Rubinstein, A. M.; Minachev, K. M. *Zeolites* **1985**, *5*, 320–324.
- (48) Grunert, W.; Hayes, N. W.; Joyner, R. W.; Shpiro, E. S.; Siddiqui, M. R. H.; Baeva, G. N. *J. Phys. Chem.* **1994**, *98*, 10832–10846.
- (49) Teraishi, K.; Ishida, M.; Irisawa, J.; Kume, M.; Takahashi, Y.; Nakano, T.; Nakamura, H.; Miyamoto, A. *J. Phys. Chem. B* **1997**, *101*, 8079–8085.
- (50) Koebel, M.; Elsener, M.; Madia, G. *Ind. Eng. Chem. Res.* **2001**, *40*, 52–59.
- (51) Ye, Q.; Wang, L.; Yang, R. T. *Appl. Catal., A* **2012**, *427–428*, 24.
- (52) Metkar, P. S.; Harold, M. P.; Balakotaiah, V. *Appl. Catal., B* **2012**, *111–112*, 67.
- (53) He, Z.; He, C.; Gao, E. Q.; Wang, Z. M.; Yang, X. F.; Liao, C. S.; Yan, C. H. *Inorg. Chem.* **2003**, *42*, 2206–2208.
- (54) Maensiri, S.; Laokul, P.; Klinkaewnarong, J.; Phokha, S.; Promarak, V.; Seraphin, S. *Optoelectron. Adv. Mater.* **2008**, *2*, 161–165.
- (55) Liu, G. *Int. J. Electrochem. Sci.* **2011**, *6*, 2162–2170.
- (56) Korhonen, S. T.; Fickel, D. W.; Lobo, R.; Weckhuysen, B. M.; Beale, A. M. *Chem. Commun.* **2011**, *47*, 800.
- (57) McEwen, J.-S.; Anggara, T.; Schneider, W. F.; Kispersky, V. F.; Miller, J. T.; Delgass, W. N.; Ribeiro, F. H. *Catal. Today* **2012**, *184*, 129.
- (58) Kispersky, V. F.; Kropf, A. J.; Ribeiro, F. H.; Miller, J. T. *Phys. Chem. Chem. Phys.* **2012**, *14*, 2229.
- (59) Brandenberger, S.; Krocher, O.; Tissler, A.; Althoff, R. *Catal. Rev.* **2008**, *50*, 492–531.
- (60) Suzuki, K.; Sano, T.; Shoji, H.; Murakami, T.; Ikai, S.; Shin, S.; Hagiwara, H.; Takaya, H. *Chem. Lett.* **1987**, 1507–1510.

- (61) Sano, T.; Suzuki, K.; Shoji, H.; Ikai, S.; Okabe, K.; Murakami, T.; Shin, S.; Hagiwara, H.; Takaya, H. *Chem. Lett.* **1987**, 1421–1424.
- (62) Kröcher, O.; Devadas, M.; Elsener, M.; Wokaun, A.; Söger, N.; Pfeifer, M.; Demel, Y.; Mussmann, L. *Appl. Catal., B* **2006**, 66, 208–216.
- (63) Rahkamaa-Tolonen, K.; Maunula, T.; Lomma, M.; Huuhtanen, M.; Keiski, R. L. *Catal. Today* **2005**, 100, 217–222.
- (64) Sun, Q.; Gao, Z. X.; Chen, H. Y.; Sachtler, W. M. H. *J. Catal.* **2001**, 201, 89–99.
- (65) Yeom, Y. H.; Henao, J.; Li, M. J.; Sachtler, W. M. H.; Weitz, E. J. *Catal.* **2005**, 231, 181–193.
- (66) Fedeyko, J. M.; Chen, B.; Chen, H. Y. *Catal. Today* **2010**, 151, 231–236.
- (67) Hadjiivanov, K.; Tsyntsarski, B.; Nikolova, T. *Phys. Chem. Chem. Phys.* **1999**, 1, 4521–4528.
- (68) Szanyi, J.; Kwak, J. H.; Moline, R. A.; Peden, C. H. F. *Phys. Chem. Chem. Phys.* **2003**, 5, 4045–4051.
- (69) Aschi, M.; Grandinetti, F. *Chem. Phys. Lett.* **1997**, 267, 98–104.
- (70) Egsgaard, H.; Carlsen, L.; Madsen, J. O. *Chem. Phys. Lett.* **1994**, 227, 33–38.
- (71) Kulkarni, S. A.; Pundlik, S. S. *Chem. Phys. Lett.* **1995**, 245, 143–149.
- (72) Abourachid, H.; Pouchan, C.; Chaillet, M. *Chem. Phys.* **1984**, 90, 243–255.
- (73) Abourachid, H.; Pouchan, C. *J. Mol. Struct.: THEOCHEM* **1985**, 22, 299–304.
- (74) Casewit, C. J.; Goddard, W. A. *J. Am. Chem. Soc.* **1982**, 104, 3280–3287.
- (75) Egsgaard, H.; Carlsen, L.; Weiske, T.; Sulzle, D.; Schwarz, H. *Chem. Phys. Lett.* **1992**, 199, 643–647.
- (76) Yuan, R. M.; Fu, G.; Xu, X.; Wan, H. L. *Phys. Chem. Chem. Phys.* **2011**, 13, 453–460.
- (77) Lamour, E.; Routier, S.; Bernier, J. L.; Catteau, J. P.; Bailly, C.; Vezin, H. *J. Am. Chem. Soc.* **1999**, 121, 1862–1869.